limit, which was twice as high as the transition pressure for ZnODEP. □

Received 12 February; accepted 27 May 2002; doi:10.1038/nature00875.

1. Drickamer, H. G. & Frank, C. W. Electronic structure, electronic transitions, and the high pressure chemistry and physics of solids. *Annu. Rev. Phys. Chem.* **23,** 39–64 (1972).
2. Collier, C. P., Saykally, R. J., Shiang, J. J., Henrichs, S. E. & Heath, J. R. Reversible tuning of silver quantum dot monolayers through the metal-insulator transition. *Science* **277,** 1978–1981 (1997).
3. Henrichs, S., Collier, C. P., Saykally, R. J., Shen, Y. R. & Heath, J. R. The dielectric function of silver nanoparticle Langmuir monolayers compressed through the metal insulator transition. *J. Am. Chem. Soc.* **122,** 4077–4083 (2000).
4. Samara, G. A. & Drickamer, H. G. Effect of pressure on the resistance of fused-ring aromatic compounds. *J. Chem. Phys.* **37,** 474–479 (1962).
5. Liu, C.-Y., Pan, H.-L., Tang, H., Fox, M. A. & Bard, A. J. Effect of structural order on the dark and photocurrents in zinc octakis (β-decoxyethyl)porphyrin thin-layer cells. *J. Phys. Chem.* **99,** 7632–7636 (1995).
6. Schouten, P. G., Warman, J. M., de Haaas, M. P., Fox, M. A. & Pan, H-L. Charge migration in supramolecular stacks of peripherally substituted porphyrins. *Nature* **353,** 736–737 (1991).
7. Liu, C.-Y. & Bard, A. J. Optoelectronic properties and memories based on organic single-crystal thin films. *Acc. Chem. Res.* **32,** 235–245 (1999).
8. Liu, C.-Y. & Bard, A. J. in *Conjugated Oligomers, Polymers, and Dendrimers: From Polyacetylene to DNA* (ed. Brédas, J.-L.) 85–116 (De Boeck Université, Paris, 1999).
9. Gregg, B. A., Fox, M. A. & Bard, A. J. Photovoltaic effect in symmetrical cells of a liquid crystal porphyrin. *J. Phys. Chem.* **94,** 1586–1598 (1990).
10. Liu, C.-Y. & Bard, A. J. Optoelectric charge trapping/detrapping in thin solid films of organic azo dyes: Application of scanning tunneling microscopic tip contact to photoconductive films for data storage. *Chem. Mater.* **10,** 840–846 (1998).
11. Liu, C.-Y., Pan, H.-L., Fox, M. A. & Bard, A. J. Reversible charge trapping/detrapping in a photoconductive insulator of liquid crystal zinc porphyrin. *Chem. Mater.* **9,** 1422–1429 (1997).
12. Aust, R. B., Bentley, W. H. & Drickamer, H. G. Behavior of fused-ring aromatic hydrocarbons at very high pressure. *J. Chem. Phys.* **41,** 1856 (1964).

Acknowledgements

We thank F.-R.F. Fan for discussions. This work was supported by the National Science Foundation and the Robert A. Welch Foundation.

Competing interests statement

The authors declare that they have no competing financial interests.

Correspondence and requests for materials should be addressed to A.J.B. (e-mail: ajbard@mail.utexas.edu).

Self-regeneration of a Pd-perovskite catalyst for automotive emissions control

Y. Nishihata*, J. Mizuki*, T. Akao*†, H. Tanaka‡, M. Uenishi‡, M. Kimura§, T. Okamoto†§ & N. Hamada‖

* *Synchrotron Radiation Research Center, Japan Atomic Energy Research Institute, Mikazuki, Sayo-gun, Hyogo 679-5148, Japan*
‡ *Materials R&D Division, Technical Center, Daihatsu Motor Co. Ltd, Ryuo, Gamo-gun, Shiga 520-2593, Japan*
§ *Materials Analysis & Evaluation Division, Toyota Central R&D Laboratories Inc., Nagakute, Aichi-gun, Aichi 480-1192, Japan*
‖ *Faculty of Science and Technology, Tokyo University of Science, Noda, Chiba 278-8510, Japan*

Catalytic converters are widely used to reduce the amounts of nitrogen oxides, carbon monoxide and unburned hydrocarbons in automotive emissions. The catalysts are finely divided precious-metal particles dispersed on a solid support. During vehicle use, the converter is exposed to heat, which causes the metal particles to agglomerate and grow, and their overall surface area to decrease. As a result, catalyst activity deteriorates. The problem has been exacerbated in recent years by the trend to install catalytic converters closer to the engine, which ensures immediate activation of the catalyst on engine start-up, but also places demanding requirements on the catalyst's heat resistance. Conventional catalyst systems thus incorporate a sufficient excess of precious metal to guarantee continuous catalytic activity for vehicle use over 50,000 miles (80,000 km). Here we use X-ray diffraction and absorption to show that $LaFe_{0.57}Co_{0.38}Pd_{0.05}O_3$, one of the perovskite-based catalysts investigated[1–4] for catalytic converter applications since the early 1970s, retains its high metal dispersion owing to structural responses to the fluctuations in exhaust-gas composition that occur in state-of-the-art petrol engines[5]. We find that as the catalyst is cycled between oxidative and reductive atmospheres typically encountered in exhaust gas, palladium (Pd) reversibly moves into and out of the perovskite lattice. This movement appears to suppress the growth of metallic Pd particles, and hence explains the retention of high catalyst activity during long-term use and ageing.

A state-of-the-art automotive petrol engine is operated close to the stoichiometric air-to-fuel ratio (by using an oxygen sensor and a sophisticated feedback control system linked to the catalyst) in order to convert simultaneously three pollutant emissions—carbon monoxide (CO), hydrocarbons, and nitrogen oxides (NO_x)[5]—into carbon dioxide (CO_2) water (H_2O) and nitrogen (N_2). A time lag associated with adjusting the air-to-fuel ratio results in a redox fluctuation in the exhaust gas. We designed our catalyst system to react to this fluctuation, to achieve greater efficiency and to conserve precious metals.

The conversion of CO and NO_x is equal at the CO–NO_x cross-over point (see Methods for catalytic evaluation), and the conversion at this point is generally accepted as a useful indicator of catalytic activity[6]. Figure 1 compares the activity of two catalysts using this indicator; one is $LaFe_{0.57}Co_{0.38}Pd_{0.05}O_3$ (Pd-perovskite, our 'intelligent' catalyst), and the other is Pd-impregnated γ-Al_2O_3 (Pd/alumina, the conventional catalyst; see Methods for catalyst preparation and testing). The Pd-perovskite catalyst maintains its high activity during ageing, whereas the activity of the Pd/alumina catalyst deteriorates by about 10%. (See Supplementary Information Fig. 1 for details on the conversion of different pollutants during the sweep test.) Imaging of the aged catalysts by transmission electron microscopy showed that the Pd particles on alumina reached sizes of up to 120 nm, whereas only small metallic particles about 1–3 nm in diameter were found on the perovskite surface (see Supplementary Information Fig. 2). X-ray energy dispersion analysis indicated that the small particles contain not only Pd, but also

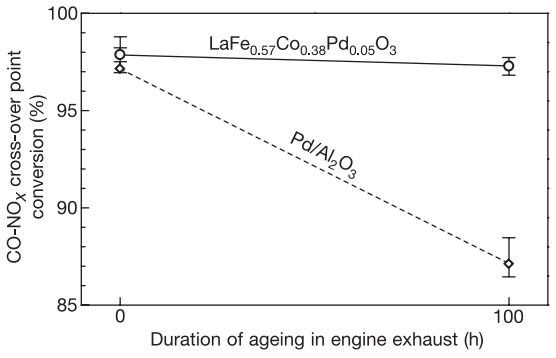

Figure 1 Change in catalyst activity during ageing. Shown is the ageing dependence of the CO–NO_x cross-over point conversion for $LaFe_{0.57}Co_{0.38}Pd_{0.05}O_3$ (Pd-perovskite catalyst) and Pd-impregnated γ-Al_2O_3 (Pd/alumina catalyst). The conversion efficiency was evaluated three times for each sample by the sweep test (see Methods). The median of the CO–NO_x cross-over point conversion (see Methods) is plotted as the symbol, together with the maximum and the minimum as error bars.

† Present addresses: Faculty of Engineering, Tottori University, Tottori 680-8552, Japan (T.A.); Research Institute for Science and Technology, Chubu University, Kasugai, Aichi 487-8501, Japan (T.O.).

Co. The remarkable suppression of metallic particle growth directly affects the capability of the Pd-perovskite catalyst to maintain high catalytic activity.

To investigate why the growth of Pd particles is suppressed on the Pd-perovskite catalyst, we conducted X-ray anomalous diffraction (XAD)[7] and X-ray absorption fine structure (XAFS)[8] measurements on oxidized, reduced and re-oxidized catalysts. The measurements were not conducted *in situ* or on samples treated in the presence of petrol exhaust; instead, the samples were simply oxidized in air, reduced by treatment in a hydrogen/nitrogen mixture, and re-oxidized in air. We expect that the structural changes seen in these samples will be similar to those occurring in the catalysts exposed to exhaust emissions in principle, but some differences may exist.

Figure 2a shows the powder diffraction pattern for the three $LaFe_{0.57}Co_{0.38}Pd_{0.05}O_3$ samples, for the limited range of momentum transfer Q that allows us to infer structural changes. Two Bragg peaks from the perovskite catalyst are assigned to the pseudocubic cell of the perovskite structure ABO_3, where A and B cations are in 12-fold and 6-fold coordination, respectively. The positions of the Bragg reflections (100) and (110) for the reduced catalyst occur at lower angles than do the corresponding reflections for the oxidized catalyst, indicating expansion of the crystal lattice. Five additional peaks appeared in the spectrum of the reduced catalyst, which were assigned to lanthanum oxide (La_2O_3) and lanthanum hydroxide ($La(OH)_3$). The spectrum indicates that the perovskite crystal structure is predominant, and that the material has partially transformed into $La(OH)_3$ through La_2O_3. The fraction of transformed material is difficult to estimate, but the X-ray absorption near edge structure (XANES) spectra at the Co K-edge imply that about half the Co, and thus about 20% of the perovskite, was transformed (see Supplementary Information Fig. 3). This quantity should depend on the reduction conditions. In the spectrum of the re-oxidized catalyst, the (100) and (110) reflections appear again at the same position as seen in the spectrum of the oxidized sample, while the extra peaks assigned to La_2O_3 and $La(OH)_3$ have disappeared completely. These results indicate that the catalyst retains a predominantly perovskite structure throughout the oxidation, reduction and re-oxidation cycle, and that similar structural changes are likely to occur during the ageing experiment.

XAD was used to determine the distribution of Pd in the catalyst. The structure factors for the pseudocubic cell are expressed approximately in the form: $F(100) \propto |f_A - f_B - f_O|$ and $F(110) \propto |f_A + f_B - f_O|$, where f_A, f_B and f_O are atomic scattering factors for the A-site, B-site and oxygen atoms, respectively. Figure 2b and c represents the energy dependence of the reflection intensity for the oxidized catalyst. The cusp of the intensity of these reflections at the Pd K-edge indicates that Pd forms a solid solution with the perovskite crystal. Furthermore, by considering the structure factors involved, the increase of (100) and the decrease of (110) reflection intensities at the edge energy prove that Pd occupies the B-site. On the other hand, the cusp of the intensity was not observed for the reduced catalyst, implying that Pd does not occupy any site in the perovskite lattice of the reduced catalyst.

The valence state of Pd can be estimated from the XANES spectrum. Figure 3a shows the XANES spectra for Pd-perovskite samples after oxidation, reduction and re-oxidation, together with the XANES spectra of PdO and a Pd foil as reference materials. Compared to the PdO spectrum, the two oxidized samples show a chemical shift of about 1.7 eV, indicating that the valence of the Pd

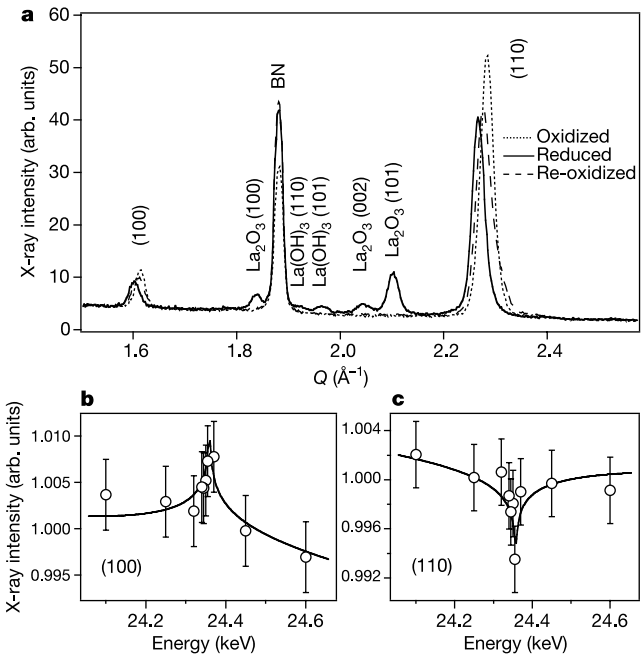

Figure 2 X-ray powder diffraction of $LaFe_{0.57}Co_{0.38}Pd_{0.05}O_3$. **a**, Diffraction pattern for catalyst samples oxidized in air, reduced in a hydrogen/nitrogen mixture and re-oxidized in air. The reflections of La_2O_3 and $La(OH)_3$ appear only in the reduced catalyst. **b**,**c**, Energy dependence of the intensity for (100) (**b**) and (110) (**c**) reflections near the Pd K-edge indicates that the B-site of the perovskite structure is occupied by Pd in the oxidized catalyst.

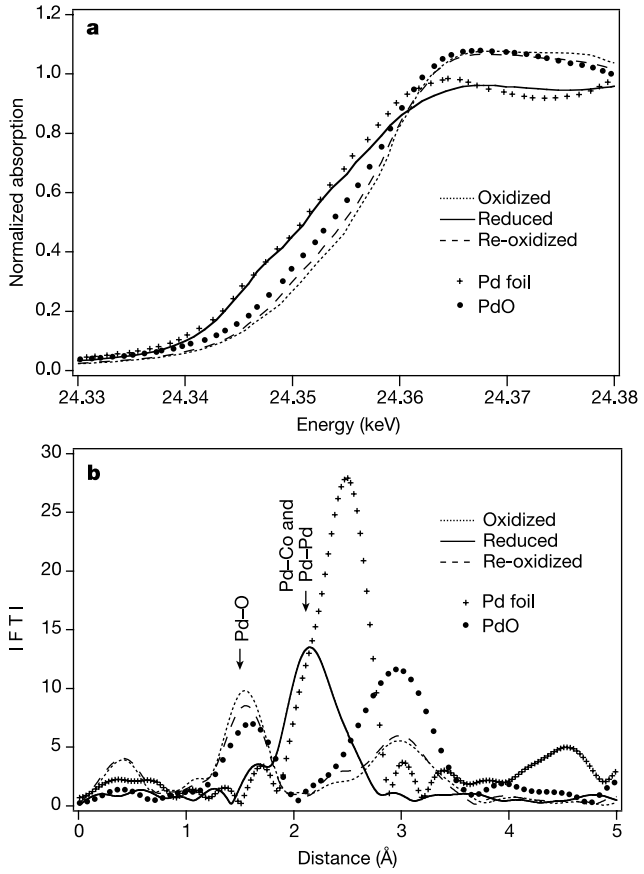

Figure 3 Comparison of XAFS data for $LaFe_{0.57}Co_{0.38}Pd_{0.05}O_3$, together with PdO and Pd foil as reference materials. **a**, XANES spectra were measured in transmission mode near the Pd K-edge. The valence state of Pd changes reversibly in a redox cycle. **b**, The radial structure function around Pd was calculated as the magnitude of the Fourier transform (FT) of the k^3-weighted EXAFS oscillations. Generally, neighbours appear closer to the X-ray absorbing atom because the phase shift of the photoelectron was not taken into account. The first-nearest neighbour of Pd is indicated by an arrow for three catalysts. The local structure around Pd atom also changes reversibly.

Table 1 Local structure parameters around Pd estimated by EXAFS analysis

Sample	Shell	Coordination number	Interatomic distance (Å)	Debye–Waller factor (Å^2)	Discrepancy factor (%)
Oxidized catalyst	Pd–O	6*	2.023(4)	0.0046(2)	4.8
Reduced catalyst	Pd–Pd	5.2	2.661(2)	0.0069(1)	6.4
	Pd–Co	6.8			
Re-oxidized catalyst	Pd–O	6*	2.032(4)	0.0056(3)	6.0
PdO	Pd–O	4*	2.040(4)	0.0034(3)	6.4
Pd foil	Pd–Pd	12*	2.743(1)	0.0067(1)	4.2

The parameters marked with an asterisk were fixed. The sum of each shell coordination number for the reduced catalyst was fixed to 12 in consideration of a disordered f.c.c. structure. The coordination number of Pd–Pd bonding is larger than expected from the concentration of Pd and Co in the sample. This implies that all of the Co atoms did not segregate out from the perovskite crystal, or that Pd atoms associate preferentially with other Pd atoms. The discrepancy factor is defined as $\sum(k^3\chi_{obs} - k^3\chi_{calc})^2/\sum(k^3\chi_{obs})^2$, where k, χ_{obs} and χ_{calc} are the wavenumber of a photoelectron excited from the X-ray absorbing atom, experimental and theoretical EXAFS functions, respectively.

in these materials is higher than the normal bivalence seen in PdO. The edge position of the reduced sample is identical to that of the Pd foil, suggesting that Pd is in a metallic state.

To elucidate the electronic state of Pd, we have performed first-principles electronic band structure calculations for Pd metal and an ordered La_2PdCoO_6 perovskite (the model material for our catalyst and based on $LaCoO_3$), by using the full-potential linearized augmented plane wave method in the local density approximation[9,10]. The calculation shows that the empty Pd 5*p* density of states is lowered and broadened on going from La_2PdCoO_6 to Pd metal, which explains the change of the experimental XANES profile among the three catalysts. In La_2PdCoO_6, the Pd 4*d* e_g band is filled partially by just one electron; like Co, Pd at the B-site is therefore trivalent. Metal ions are known to be able to exist in such unusual oxidation states in the perovskite structure by ion substitution[11–13].

The radial structure function around Pd was calculated by Fourier transform of extended X-ray absorption fine structure (EXAFS) oscillations (Fig. 3b). The local structure parameters concerning the first nearest neighbour of Pd were evaluated by nonlinear least squares fitting (Table 1). The interatomic distance between Pd and O for the oxidized catalyst sample is close to half the lattice constant for the pseudocubic cell (1.94 Å). The ionic radii of Pd^{2+}, Pd^{3+} and Pd^{4+} with six-fold coordination were reported to be 0.86 Å, 0.76 Å and 0.62 Å, respectively[14]. As the ionic radius of O^{2-} is 1.40 Å (ref. 14), trivalent or tetravalent Pd is expected from consideration of the interatomic distance in Table 1. This is also consistent with the observed chemical shift of the absorption edge for the oxidized sample. The XAFS data thus support our conclusion that Pd occupies the B-site in the oxidized sample. For the reduced catalyst, the XAD and XANES measurements suggested the segregation of metallic Pd from the perovskite crystal, while the segregation of Co was implied by X-ray energy dispersion analysis. XAFS data at the Co K-edge also indicated that about half the Co left the perovskite crystal lattice and existed in a metallic state, while the remainder kept occupying the B-site (Supplementary Information Fig. 3). The fitting model for the metallic material suggests a disordered face-centred cubic (f.c.c.) lattice containing Pd and Co, as Pd is known to form a solid solution with Co in the f.c.c. structure[15] over a wide concentration range.

This model is essentially a two-shell model, consisting of Pd–Co and Pd–Pd bonds having the same length and thermal parameter (Debye–Waller factor). As seen from the interatomic distances (Table 1), the average length given by the two-shell model, which should fall between the Pd–Co and Pd–Pd bond lengths, is comparable with the sum of the atomic radii of Pd (1.376 Å) and Co (1.253 Å)[16]. The local structure of the re-oxidized sample is essentially the same as that of the oxidized sample, indicating that it can be changed in a completely reversible manner. This evidence for Pd movement suggests that Pd might also move back and forth between the B-site in the perovskite structure and the metal particle lattice site in the 'real' catalyst, when exposed to fluctuations in the redox characteristics of the emission exhaust. □

Methods

Preparation and rapid ageing of monolithic catalysts

Our Pd-perovskite catalyst, $LaFe_{0.57}Co_{0.38}Pd_{0.05}O_3$, was prepared by the alkoxide method[17,18]. This involved dissolving metal ethoxyethylates $M^{3+}(OC_2H_4OC_2H_5)_3$ (M = La, Fe and Co) in toluene. To prepare 1 mol of perovskite oxides, metal ethoxyethylates M^{3+} $(OC_2H_4OC_2H_5)_3$ (M = La, Fe and Co) were dissolved in 200 cm^3 of toluene. Precipitates containing Pd were obtained by hydrolysis with a diluted $Pd(NO_3)_2$ aqueous solution (50.89 mg cm^{-3} as Pd metal). After drying, the precursor was calcined at 700 °C for 4 h in air to obtain a perovskite powder catalyst containing Pd homogeneously. A Pd-impregnated γ-Al_2O_3 (Pd/alumina catalyst) was also prepared as a conventional standard. Each catalyst was coated on the inner walls of a monolithic honeycomb substrate (80 mm in diameter and 95 mm in length, with a grid of 64 cells per cm^2), containing the same amounts of Pd (3.24 mg cm^{-3}). In order to investigate overall lifetime performance, the two monolithic catalysts were attached to each side bank in the exhaust system of an automotive 4,000-cm^3 V8 engine for the simultaneous ageing experiment. Then the catalysts were exposed to the high-temperature exhaust gas at 900 °C for 100 h. During exposure, two exhaust gas conditions were alternated; an atmosphere with large redox fluctuations ($\Delta\lambda = \pm 4\%$ at 0.6 Hz; see below) around the stoichiometric point was applied for 870 s, then an oxidizing atmosphere for 30 s. This ageing procedure is accepted as appropriate for the simulation of a driving strategy to achieve higher fuel economy by introducing fuel cut-off during deceleration[5,6]. The parameter λ is used to define the redox atmospheres: λ = (the present air-to-fuel ratio) / (the stoichiometric air-to-fuel ratio), where $\lambda = 1$ shows the stoichiometric air-to-fuel ratio, $\lambda < 1$ means a reducing atmosphere, and $\lambda > 1$ means a oxidizing atmosphere.

Evaluation of catalytic activity

The sweep test was carried out so as to evaluate conversion of the three pollutant emissions by shifting the mean value of λ from 0.890 to 1.096 with the fluctuation $\Delta\lambda = \pm 3.4\%$ at 0.5 Hz at 400 °C in a space velocity of 35,000 h^{-1}. Conversion of CO is improved in the lean region ($\lambda > 1$), whereas the NO_x reduction occurs readily in the rich region ($\lambda < 1$). The conversion is equal for CO and NO_x near the stoichiometric point ($\lambda = 1$), which is referred as the CO–NO_x cross-over point conversion. As a state-of-the-art automotive petrol engine is operated around the stoichiometric point within an operating window[5], the CO–NO_x cross-over point conversion is an indicator for the activity of the automotive catalyst.

Thermal treatment of catalyst for X-ray measurements

This was carried out in three steps: the powdered catalyst was oxidized in air at 800 °C for 1 h, then reduced in an atmosphere of 10% H_2/90% N_2 at 800 °C for 1 h, and finally re-oxidized in air at 800 °C for 1 h. After each step, the sample was mixed with a binder of BN, and pressed to form into pellets. X-ray diffraction and XAFS measurements near the Pd K-edge (24.350 keV) were carried out at bending-magnet beamline BL14B1 of the 8-GeV synchrotron radiation source, SPring-8.

Received 5 November 2001; accepted 27 May 2002; doi:10.1038/nature00893.

1. Meadowcroft, D. B. Low-cost oxygen electrode material. *Nature* **226,** 847–848 (1970).
2. Libby, W. F. Promising catalyst for auto exhaust. *Science* **171,** 499–500 (1971).
3. Tanaka, H., Fujikawa, H. & Takahashi, I. *Perovskite-Pd Three-Way Catalysts for Automotive Applications* (SAE Paper 930251, Society of Automotive Engineers, Inc., Warrendale, Pennsylvania, 1993).
4. Tanaka, H., Fujikawa, H. & Takahashi, I. *Excellent Oxygen Storage Capacity of Perovskite-Pd Three-Way Catalysts* (SAE Paper 950256, Society of Automotive Engineers, Inc., Warrendale, Pennsylvania, 1995).
5. Heck, R. M. & Farrauto, R. J. *Catalytic Air Pollution Control: Commercial Technology* 94–102 (Van Nostrand Reinhold, New York, 1995).
6. Waltner, A. *et al. Development of Close-Coupled Catalyst Systems for European Driving Conditions* (SAE Paper 980663, Society of Automotive Engineers, Inc., Warrendale, Pennsylvania, 1998).
7. Materlik, G., Sparks, C. J. & Fischer, K. (eds) *Resonant Anomalous X-Ray Scattering* (North-Holland, Amsterdam, 1994).
8. Teo, B. K. *EXAFS: Basic Principles and Data Analysis* (Springer, Berlin, 1986).
9. Vosko, S. H., Wilk, L. & Nusair, M. Accurate spin-dependent electron liquid correlation energies for local spin density calculations: a critical analysis. *Can. J. Phys.* **58,** 1200–1211 (1980).
10. Painter, G. S. Improved correlation corrections to the local-spin-density approximation. *Phys. Rev. B* **24,** 4264–4270 (1981).
11. Watanabe, H. Magnetic properties of perovskites containing strontium. *J. Phys. Soc. Jpn* **12,** 515–522 (1957).
12. Jonker, G. H. Semiconducting properties of lanthanum-cobalt oxide. *Philips Res. Rep.* **24,** 1–14 (1969).
13. Tejuca, L., Fierro, J. L. G. & Tascon, J. M. D. in *Advances in Catalysis* (eds Eley, D. D., Pines, H. & Weisz, P. B.) Vol. 36, 237–328 (Academic, San Diego, 1989).

14. Shannon, R. D. Revised effective ionic radii and systematic studies of interatomic distances in halides and chalcogenides. *Acta Crystallogr. A* **32,** 751–767 (1976).
15. Hansen, M. (ed.) *Constitution of Binary Alloys* (McGraw-Hill, New York, 1958).
16. Emsley, J. (ed.) *The Elements* (Clarendon, Oxford, 1994).
17. Tanaka, H., Takahashi, I., Kimura, M. & Sobukawa, H. in *Science and Technology in Catalysts 1994* (eds Izumi, Y., Arai, H. & Iwamoto, M.) 457–460 (Kodansya-Elsevier, Tokyo, 1994).
18. Tanaka, H., Tan, I., Uenishi, M., Kimura, M. & Dohmae, K. in *Topics in Catalysts* (eds Kruse, N., Frennet, A. & Bastin, J.-M.) Vols 16/17, 63–70 (Kluwer Academic, New York, 2001).

Supplementary Information accompanies the paper on *Nature*'s website (http://www.nature.com/nature).

Acknowledgements

We thank M. Misono and N. Mizuno for their advice on catalyst research.

Competing interests statement

The authors declare that they have no competing financial interests.

Correspondence and requests for materials should be addressed to Y.N. (e-mail: yasuon@spring8.or.jp).

A satellite geodetic survey of large-scale deformation of volcanic centres in the central Andes

Matthew E. Pritchard & Mark Simons

Seismological Laboratory, Division of Geological and Planetary Sciences, California Institute of Technology, Pasadena, California 91125, USA

Surface deformation in volcanic areas usually indicates movement of magma or hydrothermal fluids at depth. Stratovolcanoes tend to exhibit a complex relationship between deformation and eruptive behaviour[1]. The characteristically long time spans between such eruptions requires a long time series of observations to determine whether deformation without an eruption is common at a given edifice. Such studies, however, are logistically difficult to carry out in most volcanic arcs, as these tend to be remote regions with large numbers of volcanoes (hundreds to even thousands). Here we present a satellite-based interferometric synthetic aperture radar (InSAR) survey of the remote central Andes volcanic arc, a region formed by subduction of the Nazca oceanic plate beneath continental South America. Spanning the years 1992 to 2000, our survey reveals the background level of activity of about 900 volcanoes, 50 of which have been classified as potentially active[2,3]. We find four centres of broad (tens of kilometres wide), roughly axisymmetric surface deformation. None of these centres are at volcanoes currently classified as potentially active, although two lie within about 10 km of volcanoes with known activity. Source depths inferred from the patterns of deformation lie between 5 and 17 km. In contrast to the four new sources found, we do not observe any deformation associated with recent eruptions of Lascar, Chile[4,5].

We have created radar interferograms imaging about 900 of the approximately 1,100 catalogued volcanic edifices in the central Andes[2] (Fig. 1). Included in our study are several silicic calderas and geothermal fields. Temporal coverage is variable—for some locations, ERS 1 and 2 (European Space Agency remote-sensing satellites) radar data are available from 1992 to 2000, but only four years of data are available for a few volcanoes.

We infer four major sources of deformation from the InSAR data. We find that Uturuncu, a stratovolcano in Bolivia, has a maximum deformation rate in the radar line-of-sight (LOS) direction, U_{LOS}, of 1–1.5 cm yr^{-1} (Fig. 2). An area in southern Peru about 2.5 km east of the volcano Hualca Hualca and 7 km north of the active volcano Sabancaya is inflating with U_{LOS} of about 2 cm yr^{-1}. A third inflationary source (with $U_{LOS} = 1$ cm yr^{-1}) is not associated with a volcanic edifice. This third source is located 11.5 km south of Lastarria and 6.8 km north of Cordon del Azufre on the border between Chile and Argentina, and is hereafter called 'Lazufre'. Robledo caldera, in northwest Argentina, is subsiding with U_{LOS} of 2–2.5 cm yr^{-1}. Because the inferred sources are more than a few kilometres deep, any complexities in the source region are damped such that the observed surface deformation pattern is smooth. We find no measurable deformation at volcanoes with small eruptions or fumarolic activity during the period when radar observations were made—Ubinas (in Peru) or Guallatiri, Irruputuncu and Ojos del Salado (in Chile)[6].

It is possible that other volcanoes are deforming at rates below our detection threshold. We quantify our sensitivity to deformation by comparing temporally overlapping interferograms, and by consideration of previous analyses of InSAR accuracy[7]. We estimate that we can detect a signal of 1–2 cm amplitude that is at least 10 km in spatial extent. Differentiating such a signal from atmospheric noise within a single interferogram is difficult, but is possible by comparing multiple interferograms, as well as multiple edifices within an interferogram. Owing to decorrelation of the radar signal near many of the volcano summits, our survey is not very sensitive to localized near-surface deformation, as seen for example in the Galapagos[8]. Because the longest interferograms that we can form for most regions span about 5 yr (limited by data availability and maintaining interferometric coherence), we can detect average deformation rates exceeding 4 mm yr^{-1}.

We model the observed surface deformation as resulting from a spherical point-source of volume change, embedded in either a homogeneous or layered elastic crust. For each volcano, we simultaneously invert data from as many different time periods and satellite tracks as possible, assuming a single source location. We solve for the volume change in each interferogram separately. For our inversions, we use the Neighbourhood Algorithm global search approach, which can find multiple local minima and a range of acceptable models[9]. The misfit function is usually peaked near the best estimate, but because of the data noise and non-uniqueness of the problem, we instead choose to use the width of the misfit function to estimate a range of acceptable values.

We consider how three different seismically derived one-dimensional layered elastic models[10,11] affect estimates of source parameters. We incorporate the effects of topography upon source depth by using a different source depth for each pixel depending upon local elevation[12]. Our experiments with different elastic structures, topography, and the trade-off between source depth and volume change indicate a range of possible source depths for each centre of deformation spanning a few kilometres.

From north to south, the inferred source depths (below sea level) are: 11–13 km at Hualca Hualca; 15–17 km for Uturuncu; 6–8 km for Lazufre; and 4.5–6 km at Robledo. Thus, we find no obvious pattern in source depth within this volcanic arc. The fit of the models to the data is generally good (root mean square, r.m.s. < 1 cm, Fig. 2), although a consistent residual northeast of Hualca Hualca might indicate localized subsidence, and the oblong shape of the Lazufre deformation pattern suggests the need for a non-spherical source.

The rate of volume change seems to be time-dependent at Uturuncu, Lazufre and Robledo, whereas the deformation rate at Hualca Hualca seems constant within measurement error (Fig. 3). At Lazufre, no deformation is apparent before early 1998 in two averaged interferograms, but there is a clear signal in three later interferograms. The temporal coverage is insufficient to resolve whether the start of deformation was abrupt or gradual. At Uturuncu, there is also a slight increase in inflation rate after early